

Potential energy as a new approach for detection and monitoring of fatigue damage in scarf adhesive joints modified with nanoparticles

Journal of Composite Materials
 2022, Vol. 56(14) 2279–2298
 © The Author(s) 2022
 Article reuse guidelines:
sagepub.com/journals-permissions
 DOI: 10.1177/00219983221091871
journals.sagepub.com/home/jcm



Usama A. Khashaba^{1,2}

Abstract

In this study, fatigue results of the scarf adhesive joints (SAJs) were extensively analyzed regarding the effect of the adhesive materials (neat epoxy (NE), and SiC and Al_2O_3 -nanocomposite), bond thickness (0.17 mm and 0.25 mm) on their dynamic properties, which include loss factor ($\tan \delta$), loss modulus (E''), dissipated energy (U_d), potential energy (U_p), and storage modulus (E'). Safe fatigue lives of the NE, SiC, and Al_2O_3 -SAJs were estimated at different reliability levels. The experimental measurements revealed that reducing the adhesive layer thickness from 0.25 mm to 0.17 mm result in enhancing the tensile strength and stiffness of the SiC-SAJs by 9.6% and 4.4%, respectively, in return of 9.5% and 5.4% for the Al_2O_3 -SAJ relative to the NE-SAJ. The strength and stiffness of the SiC-SAJs with 0.17 mm bond thickness are higher than those of the Al_2O_3 -SAJ by 15.4% and 3.3%, respectively. The highest improvement of 22.0% in the fatigue strength was occurred for the SiC-SAJ with bond thickness of 0.17 mm in return of 4.8% for the Al_2O_3 -SAJ. The U_p was used for the first time (except author works) for monitoring and predicting the damage in the adhesive joints practically the change in the enclosed area of the hysteresis loop is too small to cause a large variation in the $\tan \delta$, E'' , and U_d . Damping factor of the NE-SAJs is marginally increased with the stress levels compared to the aggravated increase of both SiC and Al_2O_3 -SAJs. Zhang model predicts well the potential energy and storage modulus specially at higher stress levels.

Keywords

scarf adhesive joints, nano silicon carbide, cyclic stress-strain curve, stiffness degradation, potential energy

Introduction

Advanced fiber reinforced polymer (FRP) composite materials are commonly used for mechanical structure, automobile, and aerospace industries due to their high durability and lightweight.¹ In 1943, engineers at Wright Field used glass fiber reinforced polymer (GFRP) composite to build a monocoque fuselage for the Vultee BT-15 trainer.² Recently, carbon fibers reinforced polymeric (CFRP) composites have been widely used in numerous applications owing to their unique characteristics in comparison to other materials. This is a key reason why over half of both the Airbus A350 and Boeing 787 builds are made of composite materials. The Boeing 787 is 50% composites by weight and by 80% volume.³ Adhesively bonded joints are extensively used in these industries for assembly and repair of their composite structures. Accordingly, enhancing the performance of the bonded composite structures under fatigue loading remains an important topic for future research and is one of the important goals of this study.

The smoother taper surface of scarf adhesive joints (SAJs) minimizes stress concentrations arising from eccentricities in comparison with the over lapped joints. Hence, SAJs demonstrate a more uniform stress distribution along the adhesive layer. In comparison with single lap-joints (SLJs), the smooth surface of the SAJs minimize the aerodynamic contour changes, which makes it more suitable for repairs of the external structures.⁴ The insignificant

¹Mechanical Engineering Department, Faculty of Engineering, King Abdulaziz University, Jeddah, Saudi Arabia

²Mechanical Design and Production Engineering Department, Faculty of Engineering, Zagazig University, Zagazig, Egypt

Corresponding author:

Usama A. Khashaba, Mechanical Engineering Department, Faculty of Engineering, King Abdulaziz University, P.O. Box 80204, Jeddah 21589, Saudi Arabia.

Email: khashabu@zu.edu.eg, khashabu@hotmail.com

weight added to the bonded/repaired scarf structure increase their application in aerospace industries compared to the over lapped joints. Javaid et al.⁵ pointed out that the joint performance should be characterize under fatigue loading, which is the main reason for catastrophic failure of about 50% to 90% of mechanical structures.

In consideration of corrosion, weight, and stress concentration the bonded joints are preferred than bolted and/or riveted joints in which the drilled holes are always accompanied with delamination, fiber frying (burr), spalling, chipping, thermal degradation, and edge chipping^{6,7} that significantly reduce the performance of the composite materials.

The catastrophic failure under fatigue loading represents the main problem associated with the adhesively bonded joints that leave many questions open for future research.⁸ Most of the stiffness degradation models assuming that the adhesive joint behaves in a stable damage growth rate during most of the fatigue life. This assumption is applicable only when the joints are subjected to higher load levels, which often have a limited practical application. Moreira et al.⁹ pointed out that the stiffness degradation of scarf joint repairs CFRP composites exhibited stable damage growth for most of the fatigue life followed by sudden failure at the end of the test. At lower stress level (40% of ultimate strength), Shenoy et al.¹⁰ showed that the stiffness degradation of the bonded SLJs is not changed during 85% of fatigue lifetime after the crack initiation period and suddenly fractured due to acceleration of crack growth. Hence, new stiffness degradation models are still needed for predicting the fatigue life at low stress levels and differentiate between fatigue damage initiation and propagation. One of the important objectives of this study is to provide a new sensitive parameter for damage detection in bonded joints via measurements of loss modulus (E''), damping factor ($\tan \delta$), storage modulus (E'), potential energy (U_p), and dissipated energy (U_d) for each fatigue cycles, which remain surprisingly unexplored.

Improving the fatigue properties (strength and life) of bonded joint via infusion of nanoparticles into the adhesive layer is a recent technique, and one of the objectives of this unique study. Paygozar and Sadigh¹¹ reported that incorporation of 2 wt% nano-silica into the adhesive layer of the bonded joints enhancing their properties by 21% compared to that fabricated from pure epoxy. Marşavina and Linul¹² found that infusion of 1.0 wt% SiC nanoparticles into polyurethane foam enhanced the compressive and flexural properties by 50%–70%. Zamani et al.¹³ found that the maximum tensile strength of the modified epoxy with graphene and silica nanoparticles were obtained at 1.0wt% and 1.5wt%, respectively. The highest tensile strength and fatigue lives were obtained by the modified adhesive joint with 1.5wt% silica nanoparticles. Chavooshian et al.¹⁴ found that the shear and tensile strengths of the bonded

joints increased with insertion of nanofillers up to 1.5 wt%. This weight percent of nanofillers equal to the concentration of SiC and Al₂O₃-nanoparticles that used earlier by Khashaba et al.^{15,16} and in this study. The thickness of the adhesive layer has a detrimental effect on the mechanical properties of the adhesive joints.¹⁷ The numerical results of Liao et al.¹⁸ demonstrate that the ultimate tensile loading of the scarf adhesive joint increases as the adhesive thickness decreases. Numerical analysis of Rafiee and Taheri¹⁹ demonstrates that the optimum bond thickness of the adhesive joints ranges from 0.1 to 0.2 mm.

This paper is a continuation to those earlier studies^{16,20,21} on SAJs in CFRP composites. The tensile, fatigue, and dynamic parameters of the SAJs with adhesive thickness of 0.17 mm and modified by SiC-nanoparticles will be determined experimentally. The results will be compared with those having 0.25 mm thickness,²⁰ unmodified joints,²¹ and those modified with Al₂O₃-nanoparticles.¹⁶ Scatter in fatigue lives of the composite joints cannot be avoided even they have fabricated at the same identical conditions. Hence, in this study the Two parameter Weibull function was used to analysis the scatter in the fatigue lives of the SAJs. In addition, the S-N curves were drawn at different reliability levels to guarantee that the structure survives its function for a prescribed period of time. This will save material (in turn cost) and weight (in turn fuel consumption) compared to selecting stress level to ensure that the joint will never fail.

Experimental Work

Materials

Plain woven CFRP composite adherends [0°]₂₅ of 5 mm thickness were manufactured from 25-layer of T300-3k CFs (200 g/m²) and YPH-120-23 A/B epoxy resin using prepreg by CHN Carbon Fiber Technology Ltd. Epocast adhesive (50-A1/946), was used for bonding the composite adherends. The adhesive was supplied by Huntsman Advanced Materials. The optimum weight percent of 1.5wt% SiC-nanoparticles was used to modify the adhesive material, as determined by Khashaba et al.¹⁵ and some researchers^{13,14} based on the maximum improvement in the mechanical properties of bulk adhesive. Table 1 illustrates the mechanical properties of the composite laminate and the different bulk adhesives.

Joint fabrication and testing

The SAJs were fabrication by following several steps, which are extensively explained by Khashaba et al.^{16,21-23} and listed down as follows.

- Fabrication of the CFRP composite laminates with dimensions of 500 x 500 x 5 mm³,

Table 1. Mechanical properties of the bulk adhesives and CFRP adherends

Properties	Adhesives ^{15,16}					
	NE	SiC-nanocomposites	Gain/Loss (%)	Al ₂ O ₃ - nanocomposites	Gain/Loss (%)	CFRP adherends
Tensile strength (MPa)	75.53	78.55	4.0	75.88	0.46	895.28
Tensile modulus (GPa)	3.43	4.11	19.8	3.68	6.8	81.66
Poisson's ratio	0.32	0.318	-0.6	0.314	-1.9	0.052
Shear strength (MPa)	50.71	53.21	4.9	53.91	5.9	145.41
Shear modulus (GPa)	1.45	1.68	15.9	1.57	7.6	6.94

- Cutting each laminate to four panels with dimensions of 500 x 125 x 5 mm³, Figure 1(a),
- Scarfing each panel with taper angle (θ) of 5° along the adherend width (500 mm),
- Cleaning the machined surface in accordance with ASTM D 2093,
- Bonding two gage foils equal to the adhesive thickness (0.17 mm) closed to the ends of the tapered surface, Figure 1(a),
- Dispersion of nanoparticles into Epoxy adhesive (50-A1) via sonication processes,
- Removing the voids from the mixture using vacuum oven at -133 Pa and 40°C for 1h,
- Adding the Epoxy hardener (946) to the mixture and stirring manually for 5 min,
- Assembly the adherend panels with dimensions of 500x194.8 mm², Figure 1(b), between two waxed glass plates,
- Distribution 50 kg dead weights on the top glass plates,
- Curing the bonded panels at room temperature for 10 days.
- Cutting 21-SAJs from each bonded panels using abrasive water jet CNC machine to dimensions of 194.8x24x5 mm³.

Fatigue and tension tests

Details about tension-tension fatigue tests on the SAJs are presented by Khashaba et al. [7,16,21,24] and briefly described in this section. The SAJs were loaded by different stress levels at frequency of 10 Hz and stress ratio of 0.1 using universal testing machine model Instron 8872 according to ASTM D3166. The SAJs were clamped using double shear test fixture, Figure 2. Mean load was utilized slowly in the static mode. Stress amplitude was applied gradually until the σ_{max} is reached within the first 100-cycles, as shown by the representative example in Figure 3 ($\sigma_{max} = 59.4$ MPa). The fatigue tests were stopped at 10^7 -cycles (fatigue limit, JIS K 7118) or joint collapse whichever comes first. Table 2 shows the values of the maximum applied stresses and the loading

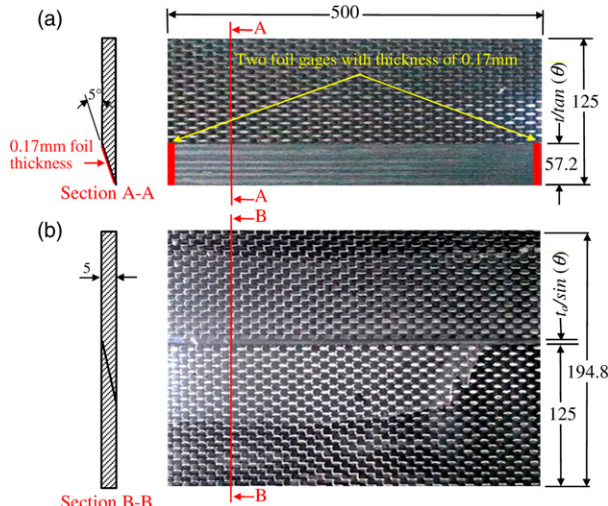


Figure 1. Dimensions of: (a) CFRP panels, and (b) bonded adherends. where t_a is the adhesive thickness (0.17 mm) and t is the laminate thickness (5 mm).

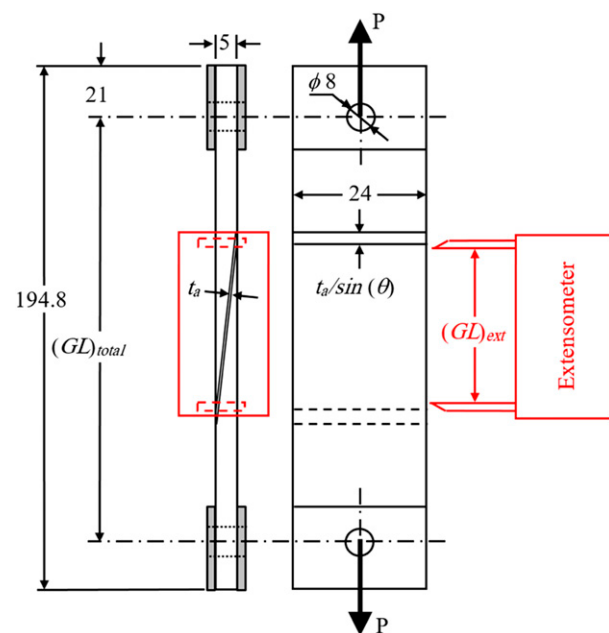


Figure 2. (a) Dimensions of the SAJs and the extensometer position.

ratio (σ_{max}/σ_u) of the NE, SiC, and Al_2O_3 -SAJs. The ultimate tensile strengths (σ_u) for the three used bonded joint materials are, respectively, 122.32 MPa, 154.28 MPa, and 133.74 MPa, as shown in Table 3 in the result and discussion section. To analyze the scatter in the fatigue results, seven SAJs were tested at each stress level. The local cyclic strain along the bondline length ($5/\tan 5^\circ = 57.15$ mm) was measured by dynamic extensometer model Instron 2620–601. The extensometer has a gauge length of 50 mm and a travel of ± 5 mm. The clamping position of the extensometer in Figure 2 was selected by many researchers^{4,16,21,23,25,26}. Hence, the measured local strain includes the strains of the adhesive layer and the adherends. Static tensile tests were performed at crosshead speed of 0.5 mm/min.

The surfaces of some SAJs were examined using Scanning Electron Microscopy (SEM) model Nova Nano SEM–230. The specimens with maximum dimensions of 5 mm was clamped on copper stubs using conductive

carbon tab and coated with thin gold layer of 1 nm/min using a vacuum evaporator for 5 min.²⁰

Data Analysis

The use of hysteresis curves is an effective approach for investigating the fatigue damage mechanisms as reported by Ameur et al.²⁷ Therefore, the stress-local strain values were recorded for each fatigue cycle during the following: 1 to 10, 20 to 100, 100 to 1000, 1000 to 10,000, 10,000 to 100,000 and from 100,000 up to failure. The increment within each interval equal to the initial range value. The last 50-cycles of the joint life were also recorded. Excel codes were developed and used to determine the dynamic parameters for each fatigue cycles. The measured dynamic parameters include dynamic stiffness, ratcheting strain, potential and dissipated energies, loss and storage moduli, and damping factor. Details on the developed Excel codes are presented by Khashaba.¹⁶

Ratcheting strain

Ratcheting strains (RS) of the SAJs under stress controlled cyclic fatigue loading can be observed due to the interfacial friction between filler/epoxy, filler/filler, and filler/CFs, which leads to softening the matrix and thus developing inelastic deformation. The ratcheting strain (ε_r) was calculated from the mean value of the maximum and minimum strains (ε_{max} and ε_{min}) along a cycle as²⁸

$$RS = \varepsilon_r = \frac{\varepsilon_{max} + \varepsilon_{min}}{2} \quad (1)$$

In this study, the relative ratcheting strain (RRS) was used to eliminate the differences in the initial values of RS (ε_r) that may be obtained when comparing the experimental results

$$RRS = \varepsilon_{rN} - \varepsilon_{r1} \quad (2)$$

where, ε_{r1} and ε_{rN} are the ratcheting strains obtained in the first and N-th cycles, respectively.

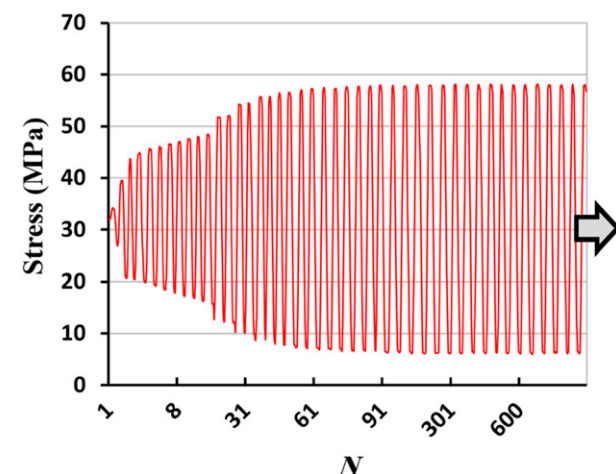


Figure 3. Evolution of stress with number of cycles of the SiC-SAJs at σ_{max} of 59.4 MPa.

Table 2. σ_{max} and load ratio (σ_{max}/σ_u) in fatigue tests.

NE-SAJs ¹⁶		SiC-SAJs		Al_2O_3 -SAJs ¹⁶	
σ_{max} (MPa)	σ_{max}/σ_u (%)	σ_{max} (MPa)	σ_{max}/σ_u (%)	σ_{max} (MPa)	σ_{max}/σ_u (%)
47.7	39.0	55.5	36.0	50.2	37.5
50.2	41.0	59.4	38.5	55.5	41.5
55.5	45.4	66.7	43.2	59.4	44.4
59.4	48.6	70.8	45.9	62.5	46.7
66.7	54.5	75.0	48.6	66.7	49.9
35-samples		35-samples		35-samples	

Table 3. Tensile properties of the SAJs with various bond thicknesses (numbers in parentheses are the standard deviation).

Joint type	Test condition		Tensile strength σ_u (MPa)	Gain, fillers %	Local modulus GPa	Gain, fillers %
	t_a (mm)					
NE-SAJ ^{16,23}	0.25 ¹⁶		102.10 (8.6)		56.47 (1.7)	
	0.17 ²³		122.32 (6.5)		58.34 (2.5)	
	Gain (%), 0.17 mm		19.8		3.3	
SiC-SAJ	0.25 ²⁰		140.75 (9.2)	37.9	64.50 (2.4)	14.2
	0.17		154.28 (7.1)	26.1	67.37 (2.8)	15.5
	Gain (%), 0.17 mm		9.6		4.4	
Al_2O_3 -SAJ ^{16,20}	0.25 ²⁰		122.11 (10.1)	19.60	55.94 (2.5)	9.5
	0.17 ¹⁶		133.74 (8.3)	9.4	65.19 (2.9)	11.7
	Gain (%), 0.17 mm		9.5		5.4	

Dynamic analysis

The schematic representation of load-displacement hysteresis loop, Figure 4, can be used to determine various dynamic parameters, which include loss modulus (E''), joint stiffness (dynamic modulus, E_{dyn}), storage modulus (E'), and damping factor ($\tan \delta$), where δ is the phase shift angle between dynamic load and dynamic displacement. The enclosed area by the hysteresis loop equal to the dissipated energy (U_d), which has a direct relationship with the developed damage in the joint.^{21,29,30} The stored elastic potential energy (U_p) in the adhesive joint equal to the area under the loading (upper) curve of the hysteresis loop, Figure 5.^{16,21,31} The U_p and the U_d can be calculated for any given cycle (N) by equations (3) and (4), respectively.^{21,27,30}

$$U_p = \frac{1}{2} \sum_{i=1}^n (d_{i+1} - d_i) [f(d_{i+1}) + f(d_i)] \quad (3)$$

$$U_d = \frac{1}{2} \sum_{i=1}^n (d_{i+1} - d_i) \{ [f(d_{i+1}) + f(d_i)] - [g(d_{i+1}) + g(d_i)] \} \quad (4)$$

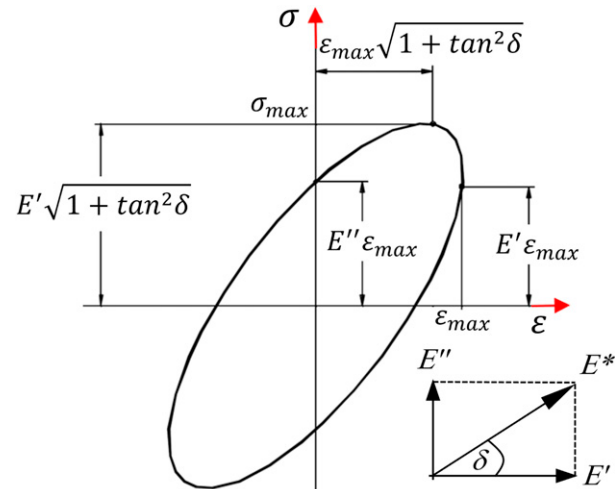
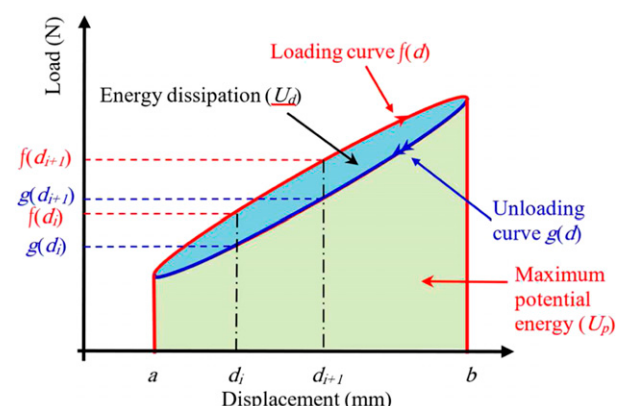
In this study, the U_p and U_d were determined through numerical integration to the area under the loading curve and the enclosed area by the load-displacement (or stress-strain) hysteresis cycles using the trapezoidal rule. Accordingly, the dynamic parameters E , E_{dyn} , E' , and $\tan \delta$ can be estimated for each fatigue cycle as follows^{16,21,30}

$$E_{dyn} = \frac{\sigma_{max} - \sigma_{min}}{\varepsilon_{max} - \varepsilon_{min}} \quad (5)$$

$$\eta = 2\zeta = \tan \delta = \frac{E''}{E'} = \frac{U_d}{2\pi U_p} \quad (6)$$

$$E' = E_{dyn} * \cos \delta \quad (7)$$

$$E'' = E_{dyn} * \sin \delta \quad (8)$$

**Figure 4.** Schematic of stress-strain hysteresis loop.**Figure 5.** Terms and nomenclatures of the potential and dissipated energies calculations.

where E_{dyn} is the dynamic modulus, ζ is the damping ratio, η is the damping factor, σ_{max} , σ_{min} , and σ_a are the maximum, minimum, and amplitude values, respectively, and ε represents the strain values of the stress cycle. These dynamic parameters (U_d , U_p , E' , E'' , E_{dyn} , and $\tan \delta$) are calculated for each recorded cycle by the developed Excel codes.²¹

Statistical Analysis of Fatigue Life Data

The fatigue life data of the adhesive joints in FRP composites always have a remarkable scatter even when the joints are prepared and tested under identical conditions.²⁰ This result was attributed to the fact that the bonded joints involve different failure mechanisms under fatigue loading. Mactabi et al.³² could not able to write a recommendation on the improvement in the fatigue results of the modified SLJs with carbon nanotubes (CNTs) because of the high scatter in their lives. The two-parameter Weibull distribution function has been successfully used earlier by Khashaba et al.²⁰ to describe the scatter in the fatigue life data of the SAJs with adhesive layer thickness of 0.25 mm that modified by different nanofillers. In the present study, the two-parameter Weibull distribution function was used to evaluate the scatter in the fatigue lives of the SAJs with different adhesive materials of 0.17 mm thickness. The Weibull probability density function $f(N_{fi})$, probabilities of failure $P(N_{fi})$, and probabilities of survival $P_s(N_{fi})$ are given by equations (9)–(11), respectively, as

$$f(N_{fi}) = \frac{\alpha}{\beta} \left(\frac{N_{fi}}{\beta} \right)^{\alpha-1} \exp \left\{ - \left(\frac{N_{fi}}{\beta} \right)^\alpha \right\}, \quad \beta \geq 0, \alpha \geq 0 \quad (9)$$

$$P_f(N_{fi}) = 1 - \exp \left\{ - \left(\frac{N_{fi}}{\beta} \right)^\alpha \right\} \quad (10)$$

$$P_s(N_{fi}) = 1 - P_f(N_{fi}) = \exp \left\{ - \left(\frac{N_{fi}}{\beta} \right)^\alpha \right\} \quad (11)$$

where α and β are, respectively, the shape and scale parameters of Weibull function, which were estimated by rewriting equation (10) as

$$\ln(N_{fi}) = \frac{1}{\alpha} \ln \ln \left(\frac{1}{1 - P_f(N_{fi})} \right) + \ln(\beta) \quad (12)$$

Equation (12) represents a straight line as: $y = bx + c$ where $y = \ln(N_{fi})$, $b = 1/\alpha$, $c = \ln(\beta)$ and $x = \ln \ln [1/(1-P_f(N_{fi}))]$. The variables in equation (12) are the measured fatigue lives (N_f), which were sorted in increasing order and the mean rank, $P_f(N_{fi})$ was computed as

$$P_f(N_{fi}) = \frac{i}{n+1} \quad (13)$$

where “ i ” is the failure order number and “ n ” is the total sample size. The values of α and β were estimated for the fatigue lives of each stress level by the least squares curve fitting. The mean life (N_m) and coefficient of variation (CV) of fatigue life data were estimated using equations (14) and (15), respectively

$$N_m = \beta \Gamma \left(1 + \frac{1}{\alpha} \right) \quad (14)$$

$$CV = \frac{\beta \sqrt{\Gamma \left(1 + \frac{2}{\alpha} \right) - \Gamma^2 \left(1 + \frac{1}{\alpha} \right)}}{N_m} \quad (15)$$

where Γ is the gamma function.

Safe fatigue life based on time to first failure concept

Safe fatigue lives were determined at different reliability levels based on time to first failure (TTFF) concept with the aid of the determined Weibull parameters. In this method, the normalized Weibull shape parameters (α_n) and scale parameters (β_n) were estimated from the normalized fatigue lives (N_f/β) for the investigated stress levels of each joint types. Safe fatigue lives (N_R) based at different reliability levels were computed as follows²¹

$$N_R = \frac{\tilde{N}}{S} = \frac{\tilde{N}}{S_M \cdot S_N \cdot S_R} = \frac{N_\gamma}{S_N \cdot S_R} \quad (16)$$

$$S_M = \left(\frac{1}{2m} X_\gamma^2(2m) \right)^{\frac{1}{\alpha_n}} \quad (17)$$

$$S_N = \left(\frac{1}{n} \right)^{\frac{1}{\alpha_n}} \quad (18)$$

$$S_R = \left(\ln \left(\frac{1}{R} \right) \right)^{\frac{1}{\alpha_n}} \quad (19)$$

$$\tilde{N} = \left(\frac{\sum_{m=1}^r x_i^{\alpha_n}}{m} \right)^{\frac{1}{\alpha_n}} \quad (20)$$

$$N_\gamma = \frac{\tilde{N}}{S_M} \quad (21)$$

where S is the scatter factor that equal to product of sample size factor (S_M), fleet size factor (S_N) and reliability factor (S_R), N_γ and \tilde{N} are the lower bound and characteristic lives, respectively. The sample size factor (S_M) represents the penalty paid to gain confidence γ (= 99%) from a finite sample size ($m = 2$, the first two lowest fatigue lives). The $X_\gamma^2(2m)$ is the chi-square distribution of $2m$ degree of freedom (the value of $X_\gamma^2(2m) = 13.277$ at confidence level

$\gamma = 99\%$ and $m = 2$,²⁰). The reliability factor (S_R) illustrates the penalty paid to gain certain reliability level (R). The penalty percentages (P) were computed at different reliability levels as follows

$$\text{Penalty paid (\%)} = 100 (N_{fp} - N_R) / N_{fp} \quad (22)$$

where N_{fp} is the estimated fatigue life using power equation (equation (23)), N_R is safe fatigue lives at different reliabilities ($N_{R=0.368}$, $N_{R=0.99}$). The first R value of 0.368 is the probability that the bonded joint will survive the characteristic life or large (substituting $N_{fi} = \beta$ in equation (11)). Thus, $P_s(N_{fi}) = R = \exp(-1) = 0.368$; in such case $S_R = 1$. In addition, the fatigue lives were estimated at higher reliability level of 0.99. Similarly, the penalties paid for the characteristic (\tilde{N}) and the lower bound lives (N_γ) can be estimated.

Results and Discussions

Tensile properties

It is obvious from Figure 6 that the tensile stress-local strain curves of the SAJs have brittle behavior up to the sudden fracture. The strength, stiffness, and toughness (area under the stress-strain curve) of the SAJs were increasing when progressing from NE to Al_2O_3 to SiC-SAJs. Table 3 shows the estimated tensile strength and local modulus based on the average of five measurements. The results in this table show that the tensile strength of the SiC-SAJs with bond thickness of 0.25 mm and 0.17 mm were improved by

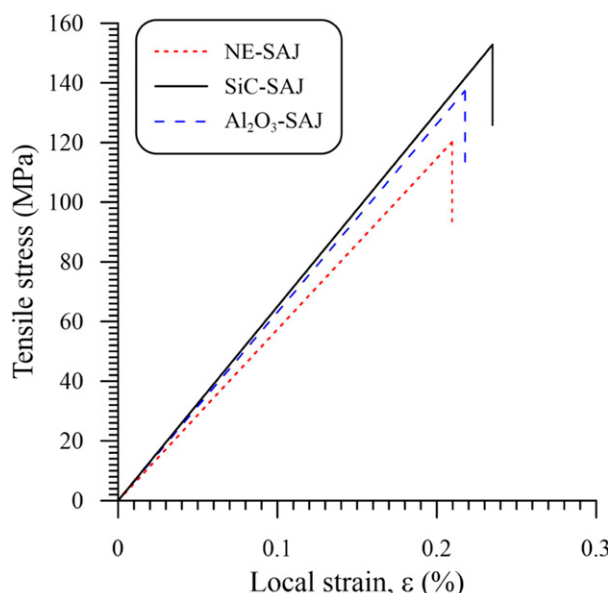


Figure 6. Representative tensile stress-strain curves of the NE and SiC-SAJs with t_a of 0.17 mm.

37.9% and 26.1%, respectively, in return of 19.6% and 9.4% for the Al_2O_3 -SAJ compared to the NE-SAJ. Reducing the adhesive layer thickness from 0.25 mm to 0.17 mm result in enhancing the strength and stiffness of the SiC-SAJs by 9.6% and 4.4%, respectively, in return of 9.5% and 5.4% for the Al_2O_3 -SAJ relative to the NE-SAJ. The strength and stiffness of the SiC-SAJs with 0.17 mm bond thickness were higher than those of the Al_2O_3 -SAJ by 15.4% and 3.3%, respectively. Hence, it can be concluded that incorporation of SiC-nanoparticles into the adhesive layer enhancing the mechanical properties (strength and modulus) of the SAJs better than the Al_2O_3 -nanoparticles. The improved properties of the modified SAJs with nanoparticles were attributed to the enhancement of the interfacial strength between the carbon fibers (CFs) on the tapered adherends and the nanocomposite adhesives as well as the improved properties of the bulk nanocomposite adhesive, as shown in Table 1.

The higher static properties (strength and local modulus) of the SAJs with thinner bond thickness (0.17 mm) was due to increasing the probability of the defects such as voids and agglomeration in the thicker adhesive layer (0.25 mm), which can act as stress riser. Agglomerations may act as stress concentrators and cause premature failure. Afendi et al.³³ reported that the apparent tensile modulus of adhesive layer of the SAJs is about 1.5–5 times higher than that of the bulk epoxy, and the strength of the joints was increased with decreasing bond thickness. Shahani and Pourhosseini¹⁷ pointed out that the increase in the adhesive thickness results in increasing stress concentration and hence, decreasing fatigue lives and strength. Numerically, Davies et al.³⁴ found that the stress state exhibited larger stress concentration factors for tensile loading in the adhesive joints with thicker bondline, which can interpret their lower strength. Moreover, the critical strain and stress at the tip ends of the SAJs are more pronounced for thicker adhesive layer, as demonstrated by the finite element analysis of some researchers.^{35,36}

Fatigue Characteristics of the scarf joints

Effect of nanoparticles and bond thickness (t_a) on the S-N relationships. Figure 7 shows comparison between the S-N curves of the NE, SiC, and Al_2O_3 -SAJs with t_a of 0.17 mm and 0.25 mm. Because of the S-N curves of the FRP composites are continues to slope downwards even after 10^8 cycles, the fatigue limits (strengths) of the SAJs were determined at 10^7 cycles, according to JIS K 7118, by the power function model as³⁷

$$\sigma_{max} = aN_f^b \quad (23)$$

where N_f is the fatigue life, a and b are the parameters of the power model.

It is clear from Figure 7 that the fatigue properties (strength and life) of the SiC-SAJs with bond thickness of 0.17 mm have remarkable increase in comparison to both NE and Al₂O₃-SAJs. Table 4 shows the estimated endurance limit (fatigue strength of the SAJs at 10⁷ cycles using power model, equation (23). The parameters of equation (23) are also included in Table 4. It is obvious from this table that the highest improvement of 22.0% was occurred in the fatigue strength due to incorporating SiC-nanoparticles into the bonded layer with 0.17 mm thickness in return of 4.8% for the Al₂O₃-SAJ. On the other hand, marginally improvement was obtained in the fatigue strength of both SiC and Al₂O₃-SAJs with adhesive layer thickness of 0.25 mm. It is worth noting that, the fatigue limits of NE, SiC, and

Al₂O₃-SAJs with bond thickness of 0.17 mm were occurred at approximately 37% of the ultimate tensile strength (σ_u), as shown in Table 4.

Reducing the adhesive layer thickness from 0.25 mm to 0.17 mm reveal a tremendous increase in the fatigue strength of the SiC-SAJs by 55% in return of 30%, and 39% for the NE and Al₂O₃-SAJs, respectively. The higher fatigue strength of the SAJs with thinner bondline thickness (0.17 mm) is related to the same reasons that mentioned in Tensile properties. In addition, the measured fatigue life of the SiC-SAJ with 0.17 bond thickness at the same σ_{max} of 59.4 MPa as example is higher than that of the NE-SAJs by about 39-times in return of 3-times for the Al₂O₃-SAJ. This result was due to the improved interfacial adhesion between the SiC-nanocomposite adhesive and the carbon fiber and thus, the strength and toughness (area under stress-strain curve) of the SiC-SAJ compared to the Al₂O₃-SAJs, as shown in Figure 6. The higher tensile and shear properties of the bulk SiC-nanocomposites, Table 1, compared to those of the Al₂O₃-nanocomposites is another reason for the higher fatigue properties (strength and life) of the SiC-SAJs. In general, the S-N curves can be used for prediction the joint life, but they do not give indication about the damage initiation, propagation, and the dynamic parameters during the lifetime of the joint that will be investigated in the following sections.

Statistical analysis. Table 5 shows the computed Weibull parameters (α and β), Mean lives (N_m) and coefficient of variation (CV%). The Weibull parameters were used to draw the Weibull fatigue life distributions of the SiC-SAJs at different stress levels, as shown by the representative example in Figure 8. It is obvious from Figure 8 that the lowest slopes (i.e., higher scatter) were observed at the intermediate stress levels (66.7 MPa and 70.7 MPa) compared to those of the minimum (55.5 MPa) and maximum (75.0 MPa) stress levels. These observations are consistent with the estimated CV% in Table 5. This behavior was attributed to changing from the distinct failure mechanisms at the minimum stress

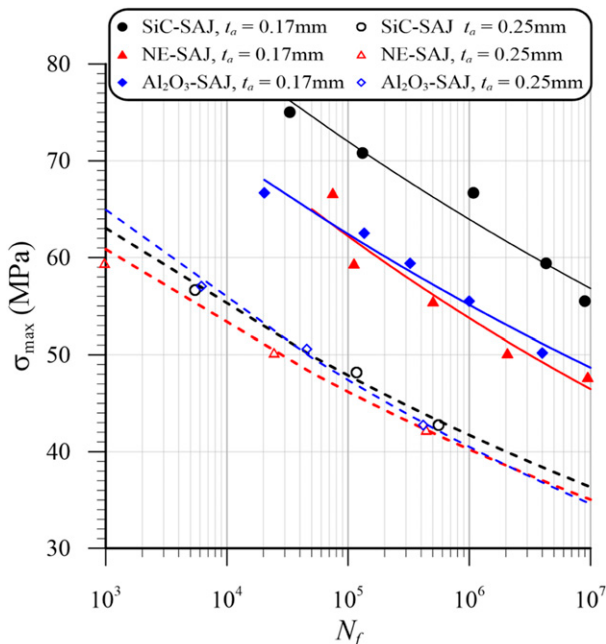


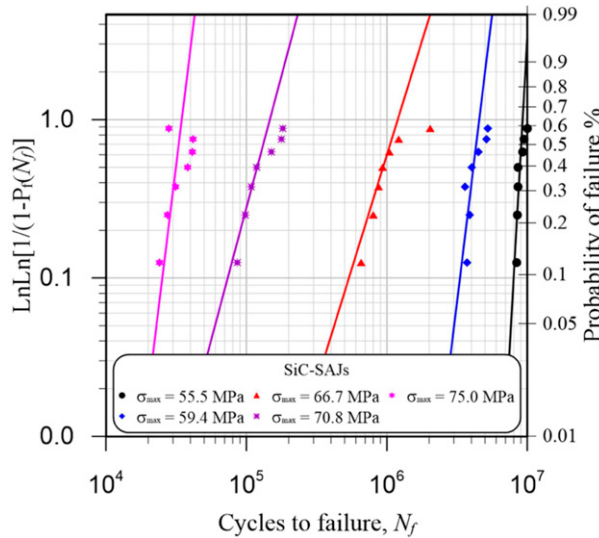
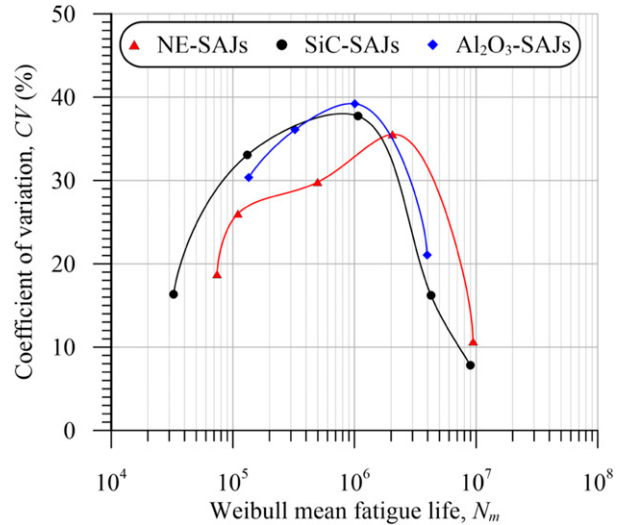
Figure 7. S-N curves of the NE and SiC-SAJs with different bondline thicknesses (t_a).

Table 4. Improvement in the endurance limits (fatigue strengths) of the SAJs.

Joint type	Adhesive thickness, t_a (mm)	Parameters of the power model, equation		σ_e at 10 ⁷ cycles (MPa)	${}^eE/\sigma_u$ (%)	Improvement (%) due to	
		a	b			Adhesive type	t_a
NE-SAJ	0.25	87.1	-0.0554	35.66	34.93		
NE-SAJ	0.17	129.03	-0.0634	46.44	37.97		30
SiC-SAJ	0.25	93.626	-0.0583	36.58	25.99	2.6	
SiC-SAJ	0.17	130.83	-0.0519	56.68	36.74	22.0	55
Al ₂ O ₃ -SAJ	0.25	99.584	-0.0648	35.04	28.70	-1.7	
Al ₂ O ₃ -SAJ	0.17	116.24	-0.054	48.68	36.40	4.8	39

Table 5. Weibull parameters and coefficient of variation (CV%) of fatigue life results.

Test temperatures	σ_{\max} (MPa)	Weibull parameters		N_m	CV%	Penalty paid (%) to gain safe lives				Normalized weibull parameters	
		α	β			\tilde{N}	N_γ	$N_{R=36.8\%}$	$N_{R=99\%}$	α_n	β_n
NE-SAJs ²¹	47.7	11.35	9,859,490	9,428,321	10.7	19.1	35.3	54.9	80.8	5.378	0.998
	50.2	3.08	2,294,624	2,051,383	35.5	20.0	36.0	55.4	81.1		
	55.5	3.74	551,972	498,436	29.8	21.8	37.4	56.4	81.5		
	59.4	4.35	121,150	110,334	26.0	23.0	38.4	57.1	81.8		
	66.7	6.21	79,747	74,123	18.8	25.0	40.0	58.2	82.2		
SiC-SAJs	55.5	15.65	9,256,855	8,950,782	7.9	12.8	30.9	52.7	80.6	5.154	1.041
	59.4	7.28	4,547,130	4,262,191	16.2	16.1	33.5	54.4	81.3		
	66.7	2.88	1,195,799	1,065,932	37.7	21.5	37.8	57.3	82.5		
	70.8	3.33	146,755	131,709	33.1	24.1	39.8	58.8	83.1		
	75	7.22	34,664	32,477	16.3	26.5	41.8	60.1	83.7		
Al_2O_3 -SAJs	50.2	5.48	4,292,336	3,961,934	21.1	34.3	49.2	66.6	87.6	4.643	0.993
	55.5	2.76	1,129,554	1,005,230	39.2	30.9	46.6	64.9	87.0		
	59.4	3.02	363,829	325,001	36.1	28.5	44.8	63.7	86.5		
	62.5	3.66	149,692	135,018	30.4	26.6	43.3	62.7	86.2		
	66.7	7.12	21,574	20,199	16.54	24.2	41.4	61.5	85.7		

**Figure 8.** Weibull fatigue life distributions of the SiC-SAJs.**Figure 9.** Coefficient of variation in fatigue lives versus number mean lives of the NE, SiC, and Al_2O_3 -SAJs.

level of 55.5 MPa (cohesive/adhesive) and maximum stress level of 75.0 MPa (interfacial) to a mixed modes the intermediate stress level (66.7 MPa and 70.7 MPa) as shown later.

Figure 9 shows the variation of $CV\%$ versus N_m of the NE, SiC, and Al_2O_3 -SAJs. It is clear from Figure 9 that the highest scatter in the fatigue data occurred at about 10^6 cycles. Similar observations were reported by Khashaba³⁸ and Tanimoto et al.³⁹ They have found that the widest scatter in the fatigue lives of GFRP composites with different fiber volume fractions observed at 10^5 to 10^6 cycles. This tendency in the scatter in the fatigue lives at varying

stress levels is extremely important and deserves much attention for the design and application of GFRP composites. The results in Figure 9 also show that the lowest scatter in the fatigue life data was observed in NE-SAJs compared to those of the SiC and Al_2O_3 -SAJs as a result of increasing the constituent materials (nanofillers). Mactabi et al.³² reported that the large scatter in the fatigue life data of the adhesive joints make it difficult to take a decision about their performance, which increases the importance of this study.

Fatigue lives of the SAJs at different reliability levels. For each joint types, the fatigue lives for the different stress levels were normalized by their Weibull scale parameter (β , Table 5). The normalized fatigue lives were used for computing the normalized Weibull parameters α_n and β_n , Table 5, and hence, the fatigue lives of the NE, SiC, and Al_2O_3 -SAJs at were computed at different reliability levels (\tilde{N} , N_y , $N_{R=0.368}$, $N_{R=0.99}$), as shown in Figure 10. It is obvious from Table 5 that the overall scatters in the fatigue life data of the Al_2O_3 -SAJs is marginally increased ($\alpha_n = 4.643$) compared to those NE and SiC -SAJs, which having higher shape parameter of 5.378 and 5.145, respectively. This result is consistent with the highest penalty paid (%) to obtain safe fatigue lives of the Al_2O_3 -SAJs compared to the NE and SiC-SAJs as shown in Table 5.

It worth noting that the S-N curve of the SiC-SAJs at the higher reliability level (99%) is higher than that at 50% survival of the Al_2O_3 -SAJs. The predicted safe fatigue life of SAJs is of considerable value to the designer with SAJs in aerospace composite structures, where the stress level can be selected based on that the structure will survival performing their functions for prescribed period as shown in the S-N curves of Figure 10. In particular, if the structure contains a critical component where any failure is catastrophic, the design criteria must consider the weakest member of the population, not the mean, mode, or other central tendency of the distribution.

Evolution of ratcheting strain versus number of cycles. Figure 11(a) shows the effect of stress level on the variation of the relative ratcheting strains (RRSs) of the SiC

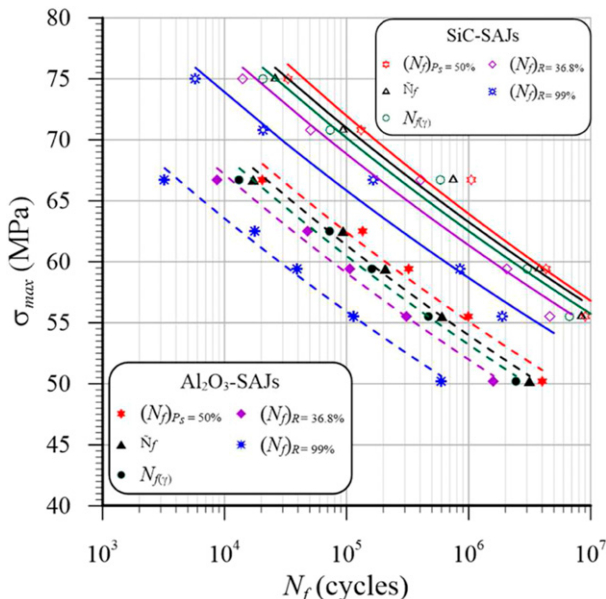


Figure 10. S-N curves of the SiC, and Al_2O_3 -SAJs at different reliability levels.

and Al_2O_3 -SAJs during fatigue cycles of some representative samples. It is obvious that the Al_2O_3 -SAJs exhibited higher RRSs compared to that of the SiC-SAJs, as shown in Figure 11(a). The higher ratcheting strains of the Al_2O_3 -SAJs are accompanied with lower fatigue lives due to the interfacial damage growth as a result of lower bonding strength between the adhesive layer and carbon fibers (CFs). At high stress levels, the values of the RRSs were aggravated due to increasing the accumulated interfacial self-heating temperatures, which were supported by the lower thermal conductivities of the CFRP adherends (0.36 W/m°C) and the adhesive layer (0.18 W/m°C).⁴⁰ The accumulated self-heating temperature leads to increasing the inelastic strain (ratcheting strain), as shown in Figure 11. The presence of the nanoparticles in the adhesive layer tend to increase the interfacial friction and thus, the RRSs as consequence of the increased interfacial self-heating temperature, compared to the fabricated joints from neat epoxy (NE) as shown in Figure 11(b). Goel et al.⁴¹ reported that, the induced self-heating temperature during fatigue tests of GFRP composites was increased by about 10°C that caused premature failure of the specimens. Although the Al_2O_3 -SAJs have approximately the same fatigue life of the NE-SAJs at stress level of 59.4 MPa, Figure 11(b), their gradual increase in the RRSs can be better modeled for predicting their lives and avoiding the sudden failure compared to the NE-SAJs. The higher RRSs of both SiC and Al_2O_3 -SAJs and their gradual increase with N could be attributed to some of the following reasons:

Failure mechanisms of the SAJs. On the macroscale level, Figure 12(a)–(c) shows representative images of the fracture surface of the SAJs with different adhesives and load levels. It is clear from Figure 12(a)–(c) that the fracture of the SAJs is dominant by mixed cohesive/adhesive/light-fiber-tear failure modes. The cracks were initiated at the ends of the joint, then propagated toward the center of the adhesive layer in form of adhesive/light-fiber-tear failure modes. The interfacial failures were jumped from one side to the other causing cohesive failure to the adhesive layer. The light-fiber-tear failure mode was characterized by cleavage appearance, as consequence of the light-fiber-tear failure modes, which can be observed visually on the tapered adherends. This is a very desirable failure mode, which demonstrates on the high interfacial bond strength. For a limited number of SAJs almost that were tested at high stress levels, and hence shorter lives, the mode of failure is dominated by interfacial failure along the bondline without cohesive failure of the adhesive layer as shown for the SiC-SAJ at 75.0 MPa, Figure 12(c).

On the microscale level, Figures 13 and 14 show representative SEM images of the fracture surface of the bulk adhesives and interfacial (taper) surface of the SAJs, respectively. It obvious from Figures 13(a) and (b) that the fracture surfaces of the modified adhesive with SiC and

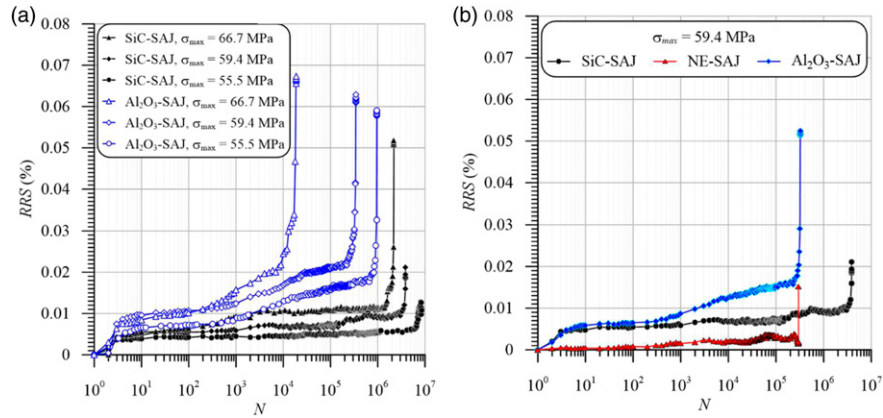


Figure 11. Evolution the RRS with N : (a) of SiC and Al₂O₃-SAJs at various σ_{max} , and (b) of the NE, SiC and Al₂O₃-SAJs at σ_{max} of 59.4 MPa as representative examples.

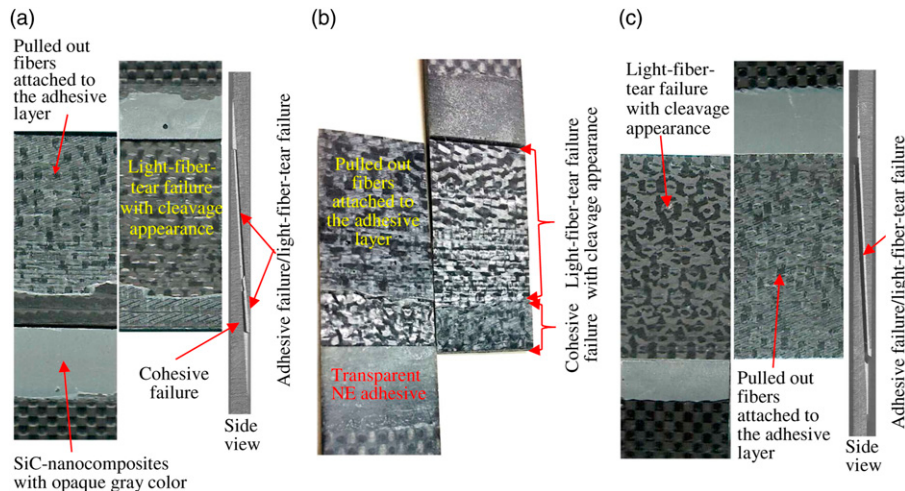


Figure 12. Representative images of fracture surfaces in fatigue tests: (a) SiC-SAJs at 55.5 MPa, (b) NE-SAJs at 55.5 MPa, and (c) SiC-SAJs at 75.0 MPa.

Al₂O₃ nanoparticles are highly rough, wavy, and rugged, with a greater number of steps and craters compared to the smoother surface of NE-adhesive, Figure 13(c). This behavior is attributed to the good interfacial bond strength between matrix and the well-dispersed hard nanoparticles that leads to propagation of crack through the matrix above or below the particles. The corrugated surface of the SiC-nanocomposites is more pronounced compared to that of the Al₂O₃-nanocomposites. Hence, the SiC-nanocomposite has the highest stiffness and toughness (area under the stress-strain curve) as shown in Figure 6. Hence, the modified joint with SiC-nanoparticles adhesive absorb more energy to perform the corrugated surface, Figure 14(a), which consistent with the improved toughness, fatigue life, and the gradually and progressively increase of the RRSs, as shown in Figure 11(b) compared to the NE-SAJs. On the other

hand, the relatively lower interfacial bond between the Al₂O₃-nanoparticles and the Epoxy adhesive result in lower level of surface corrugation, Figure 13(b), and hence lower fatigue lives. It is clear from Figure 14(b) that the SiC-nanocomposite adhesive layer is firmly attached to the CFs, which demonstrate on the higher interfacial bonding and thus, higher levels of failure stress were obtained under static, and fatigue loads, as shown in Figures 6 and 7, respectively. On the other hand, the smooth prints of the delaminated weft (transverse) CFs, Figure 14(c), demonstrates on the lower interfacial bonding strength and thereby, the NE-SAJs tend to sudden catastrophic failure without warning, Figure 11(b). For these reasons, the SiC-SAJs exhibited progressive stiffness degradation with fatigue cycles and possess higher damping characteristics relative to the NE-SAJs, as will be shown in the following sections.

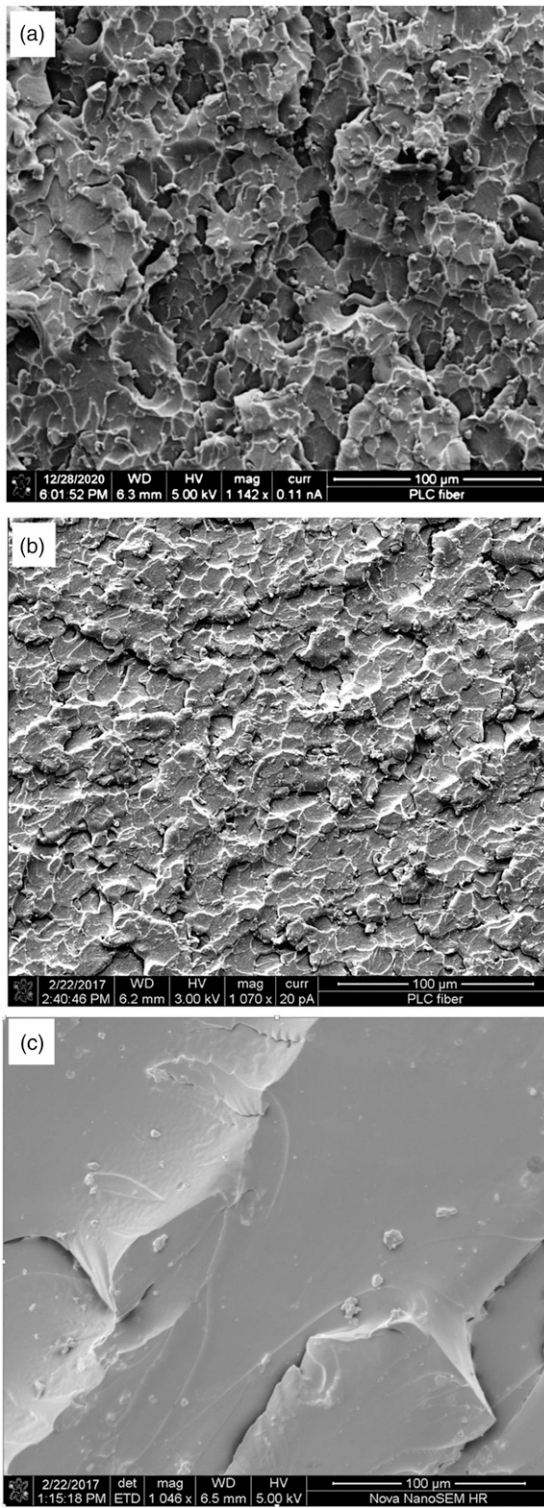


Figure 13. SEM images of the fracture surface of bulk adhesives: (a) SiC-nanocomposite, (b) Al₂O₃-nanocomposite and (c) NE.

Behavior of the stress-strain hysteresis loops. Figures 15(a)–(c) shows illustrative examples of the hysteresis loops of NE, SiC, and Al₂O₃-SAJs at 66.7 MPa. It is obvious from

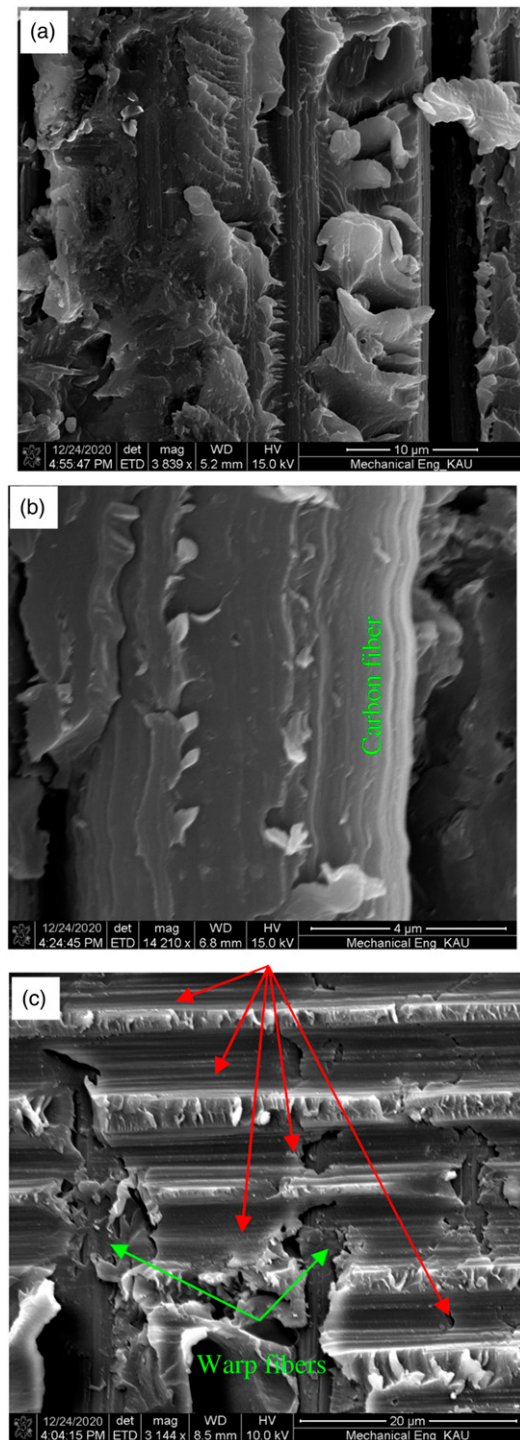


Figure 14. SEM images of taper surface of SAJs at σ_{max} of 66.7 MPa: (a) and (b) SiC-SAJs, and (c) NE-SAJ.

Figures 15(a) and (c) that the slopes of the hysteresis loops of the NE and Al₂O₃-SAJs were decreased significantly with N , as an indication to the interfacial crack growth. In addition, σ_{max} of 66.7 MPa the enclosed by the hysteresis

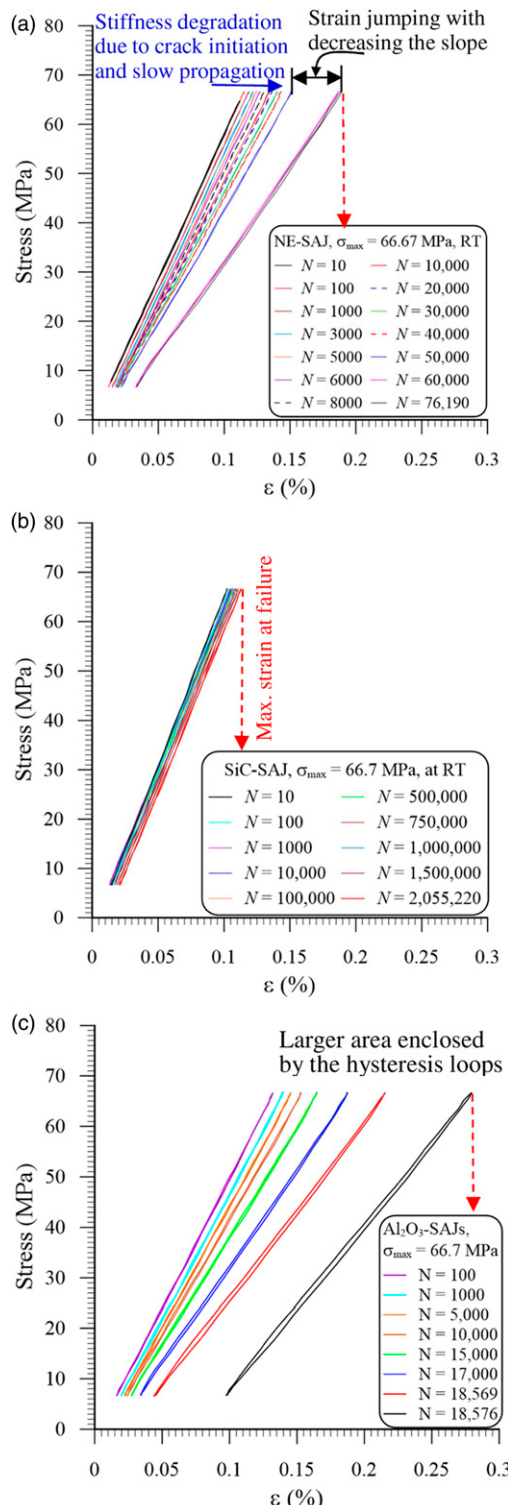


Figure 15. Samples of stress-strain hysteresis loops at σ_{max} of 66.7 MPa: (a) NE-SAJs, (b) SiC-SAJs, and (c) Al₂O₃-SAJ.

loops of the Al₂O₃-SAJs are larger compared to that of the NE-SAJs. This is a peculiar phenomenon, which consistent with the lower fatigue life of the Al₂O₃-SAJs compared to

the NE-SAJs particularly at this stress level, as shown in Figure 7. To confirm this phenomenon, it is necessary to perform fatigue tests at stress levels close to 66.7 MPa. In contrast, the slope of the stress-local strain cycles (stiffness) of the SiC-SAJs remains constant during almost the entire lifetime of the joint, Figure 15(b). The maximum failure strain of the Al₂O₃-SAJ is (0.28%) higher than those of the NE-SAJs ($\approx 0.19\%$) and SiC-SAJs (0.115%) by about 47% and 144%, respectively. The fatigue life of the SiC-SAJs (average of 7 measurements) is (1.077×10^6) higher than that of the NE-SAJs (7.47×10^4) by 14-times in return of 53-times of the Al₂O₃-SAJ is (2.033×10^4).

Stiffness degradation. Figure 16(a) and (b) shows the variation of E_{dyn} versus N/N_f of the NE, SiC, and Al₂O₃-SAJs at σ_{max} of 55.5 MPa and 66.7 MPa, as representative examples. The values of E_{dyn} were estimated from the slope of the stress-local strain hysteresis curves. The fatigue cycles (N) were normalized by the fatigue life (N_f) of each specimen. The results in Figure 16(a) and (b) show that the SiC-SAJs have the highest dynamic stiffness compared to both NE and Al₂O₃-SAJs. This result was attributed to the improved tensile strength and stiffness of the SiC-SAJs by 26.1% and 15.5%, respectively, in return of 9.4% and 11.7% for the Al₂O₃-SAJs compared to those of the NE-SAJs, as shown in Table 3. The improved interfacial bonding of the SiC-nanocomposite adhesive with CFs that was demonstrated by the SEM images of Figure 14(b), is another reason for enhancing the joint stiffness.

At low stress level of 55.5 MPa, both NE and SiC-SAJs do not exhibit any stiffness degradation up to the end of their lifetime accompanied with catastrophic without warning. On the other hand, the stiffness degradation curve of the Al₂O₃-SAJs showed three distinct damage rates. It is obvious that the stiffness degradation was increased with increasing σ_{max} , as can be observed by comparing Figure 16(a) and (b). The induced damage was aggravated with increasing σ_{max} and thus, became more effective on the stiffness reduction rate, as shown in Figure 16(b). Similar observations were reported by some researchers.^{16,21,42-45} They have found that the stiffness degradation rate of the adhesive joints is significantly dependent on the applied stress level.

The stiffness degradation curves of the Al₂O₃-SAJs (Figure 16 a and b) and both NE, and SiC-SAJs at σ_{max} of 66.7 MPa, Figure 16(b), can be divided into three different stages based on the accumulated rate of fatigue damage similar to that observed by some researchers^{26,44-46} for different composite joints. In stage I, rapid stiffness degradation was occurred during the initial fatigue cycles due to matrix cracking parallel to the warp (transverse) fibers on the tapered adherends, which are normal to the loading direction.²³ In stage II, the stiffness degradation was distinguished by a linear steady state manner. The change from the linear behavior of stage II determine the end of stage I

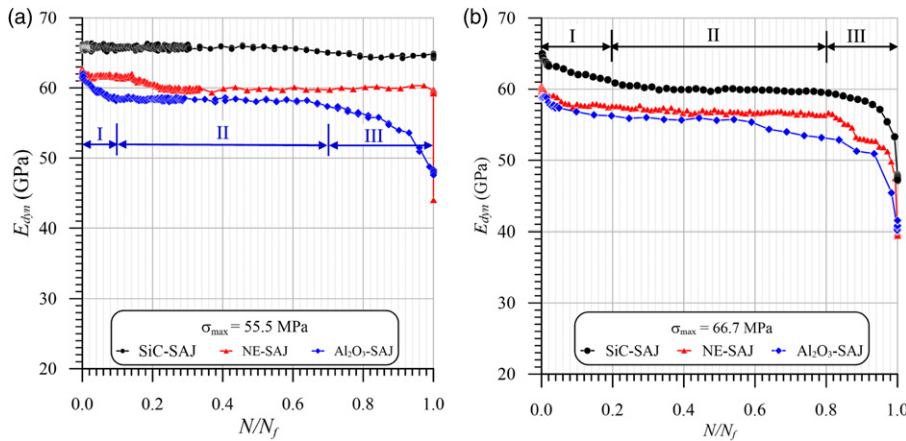


Figure 16. Dynamic modulus versus N/N_f of NE, SiC, and Al_2O_3 -SAJs: (a) $\sigma_{\max} = 55.5$ MPa, and (b) $\sigma_{\max} = 66.7$ MPa.

and the beginning of stage III, which is characterized by sharp increasing rate of the stiffness degradation followed by a catastrophic failure. This behavior is due to the interfacial crack growth and peeling of low stiffness adherend tips toward the adhesive layer center, as demonstrated by Khashaba et al.²² through the measurements of the strain distribution along the bondline and the adherend tips of the SAJs.

Embedding nanoparticles into the bond layer of the SAJ can improve its toughness to some extent due to interfacial microcrack initiation and propagation around the nanoparticles.^{47,48} This hypothesis was demonstrated by the SEM images of the corrugated fracture surface of the nanocomposites as shown in Figure 13(a) and (b), which consistent with the larger area under their tensile curves, Figure 6, compared to the net epoxy. Hence, it can be concluded that infusion of the nanoparticles in the bond layer of the SAJs improve the stiffness degradation rate with smoother behavior and thus, can be better modeled for predicting their lives compared to the fabricated joints from neat adhesive. Ding and Cheng⁴⁷ attributed the extending of stage II and fatigue life of nano-silica-reinforced CFRP composites to the improvement of matrix toughness and hence, its ability to absorb more external energy.

Zhang et al.⁴⁵ developed a non-linear sigmoid model in which the curve shows fast initial degradation rate in stage I followed by a constant degradation rate for the most lifetime of the joint in stage II, and sharp increasing degradation rate in stage III at the end of joint life

$$\frac{E(N)}{E(0)} = \left(\frac{N \cdot k^m}{V - N} \right)^{\frac{1}{m}} \quad (24)$$

where $E(N)$ is the dynamic modulus related to the N^{th} fatigue cyclic, $E(0)$ is the dynamic modulus at the first cycle

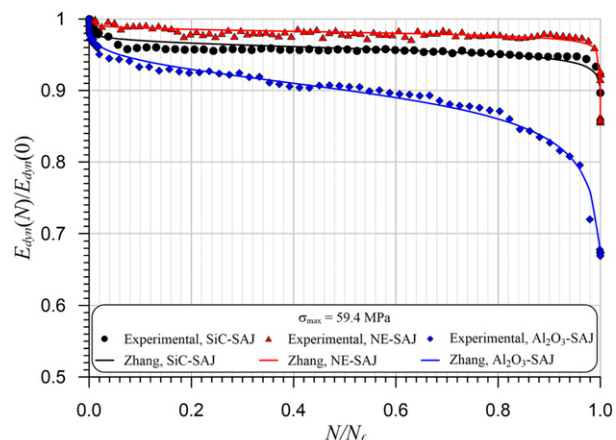


Figure 17. Normalized stiffness degradation versus N/N_f of NE, SiC, and Al_2O_3 -SAJs at σ_{\max} of 66.7 MPa.

and, k , m , V are model parameters, which were determined using Excel Solver based on minimum sum of squared errors (SSE). Similar nonlinear model was developed by Jiang et al.⁴⁴

Figure 17 shows typical normalized stiffness degradation as a function of normalized fatigue cycles of the NE, SiC, and Al_2O_3 -SAJs at σ_{\max} of 66.7 MPa. It is obvious from Figure 17 that the Al_2O_3 -SAJs exhibited a progressive stiffness degradation as a function of loading cycles. This behavior may be attributed to microcracking initiation and propagation through the adhesive layer above or below the nanoparticles. Accordingly, the fractured surface of the modified adhesive is more corrugated, Figure 15. Therefore, Zhang model predicts well the stiffness degradation of the Al_2O_3 -SAJ because it is following the sigmoid path, especially in stage II, which behave in a nearly steady state degradation (damage) growth.

Behavior of the dynamic parameters of the SAJs. Figure 18 indicates the variation of the measured dynamic parameters (E' , E'' , U_d , U_p and $\tan \delta$) versus N/N_f of the SiC-SAJs at σ_{max} of 66.7 MPa as an illustrative sample. The dissipated energy (U_d) is qualitatively agreed with both $\tan(\delta)$ and loss modulus (E'') that are scattered in a zigzag fashion without obvious trends with fatigue cycles. Based on the fact that the damping values of the engineering materials are increased with the damage level, the high strength CFRP composite adherends (895.28 MPa) are not affected by the maximum applied stress level (75 MPa) and hence, does not contribute to the overall damping. Therefore, the enclosed areas by the stress-local strain cycles are very small, which result in lower values of the dissipated energy and hence, the damping factor and phase shift angle (δ), equation (6). Accordingly, the values of E' are almost equal to the dynamic modulus, equation (7), while the values of the E'' are few thousandths of an GPa, equation (8). Similar zigzag manners were found by some investigators.^{16,21,29,49} The results in Figure 18 also show that the dissipated energy (U_d) was suddenly increased at the end of stage III as a result of increasing the accumulated interfacial thermal damage. Li et al.⁵⁰ have attributed similar behavior to the fiber/matrix debonding accompanied with interfacial frictional slipping.

The predicted stiffness degradation and potential energy of the SiC-SAs depicts relatively less agreement with the experimental results. This was due to at lower stress level, the stiffness in stage II takes a lot of time without significant degradation, as shown in Figure 15(b). Therefore, the measured values of the stiffness degradation do not follow a sigmoid curve (i.e., lower rate in stage II), as shown in Figure 18. Hence, new stiffness degradation models are always required to predict fatigue lives under low or moderate stress levels at which the failure was occurred catastrophically, without warning.

Figure 19 shows the effect of stress level on the damping factor of NE, SiC, and Al_2O_3 -SAJs. It is obvious that the damping factor of the NE-SAJs is marginally increased with the stress levels compared to the aggravated increase of both SiC and Al_2O_3 -SAJs. This is attributed to the higher energy dissipated in developing interfacial microcracks initiation ahead of nanoparticles and propagation, as shown in Figure 13(a) and (b). Increasing the accumulated interfacial friction temperature that was assisted by the lower thermal conductivities of the constituent materials can also play a key role in increasing the damping of both SiC and Al_2O_3 -SAJs via interfacial softening and slippage of the nanoparticles as well as among the nanoparticles themselves, as

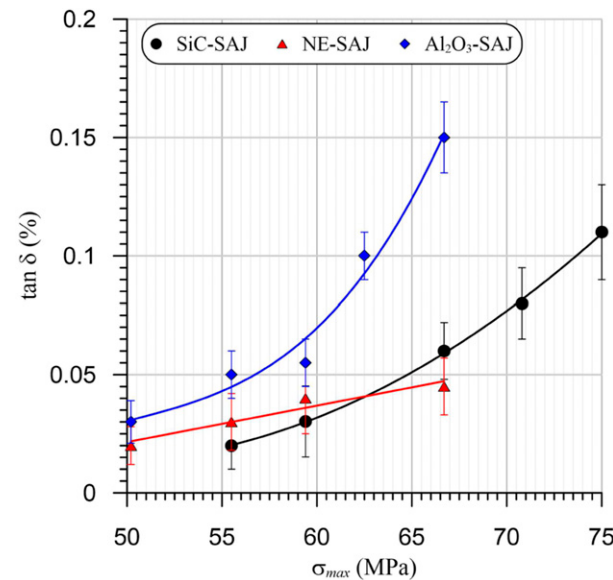


Figure 19. $\tan \delta$ versus σ_{max} .

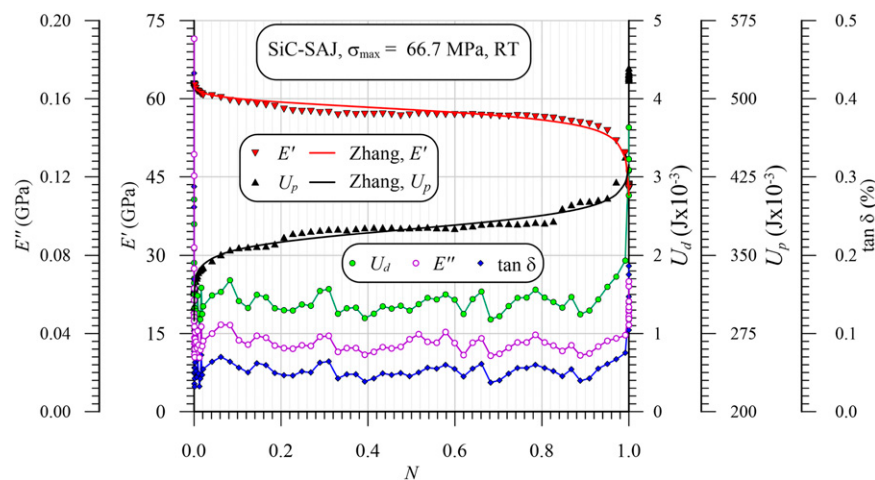


Figure 18. Dynamic parameters versus N/N_f of the SiC-SAJs at σ_{max} of 66.7 MPa.

reported by Alva and Raja.⁵¹ It is worth noting that the damping factors of the Al_2O_3 -SAJs are higher than those of the SiC-SAJs. This behavior was consistent with increasing the enclosed area by the hysteresis loops of the Al_2O_3 -SAJs, Figure 15(c), compared to both NE and SiC-SAJs and thus, decreasing their dynamic modulus, Figure 17, which has inverse relationship with $\tan \delta$, equation (6).

The current study built on the insights of Khashaba et al.^{16,52} who have validated the estimated damping factors from the developed Excel codes by fitting the measured sinusoidal stress and strain data to the following sine function

$$\sigma \text{ or } \varepsilon = a \sin(b(\theta - h)) + k \quad (25)$$

where k , a , and b are coefficients and θ is the cycle angle (0 to 2π), and h is the horizontal shift angle. When h is added to θ , the maximum stress (or strain) occurs at $\pi/2$, $3\pi/2$ and the minimum at 0, π , 2π . Hence, the phase shift angle (δ) is computed by subtracting the “ h ” values of the strain and the stress equations. Khashaba et al.^{16,52} found good agreement between the predicted phase shift angle (δ) using equation (25) and that calculated using equation (6) via the developed Excel codes.

After an extensive review of the literature, it has been found that there is no available data on the dynamic performance of the scarf adhesive joint yet except of the author works.^{16,21,24,52} Therefore, data about the damping factor ($\tan \delta$) of some different types of adhesively bonded joints are collect and compared with those of the SAJs, as shown in Table 6. It is obvious from Table 6 that the damping factors of the SAJs are in the range of some SLJs, which were determined using free vibration decay method, as shown in Table 6.

Gunawan and Gibson⁵³ reported that the $\tan \delta$ of SLJ is equal to the summation of the product of the strain energy and $\tan \delta$ of the adherend plus the summation of the product of the strain energy and $\tan \delta$ of the adhesive, all are divided by the total strain energy of the adhesive and the adherends. Hence, the lower values of $\tan \delta$ of SAJs, Table 6, were due to inability of the applied maximum load level of 75 MPa to cause a significant strain/damage in the high strength

adherends (895.28 MPa). In addition, Adams et al.⁵⁴ found that the damping factor of the adhesively bonded lap joint is about 1.6% of the damping of the adhesive material.

The values of E' of the SAJ, Figure 18, were quantitatively consistent with those of the E_{dyn} , as shown in Figure 16(b). This result was due to the very small phase shift angle (δ) between the sinusoidal stress and strain and hence, $\cos(\delta) \approx 1$ and $E' = E_{dyn}$, equation (7). The results in Figure 18 also show that E' behave in opposite manner in comparison with the U_p and both can be used to monitor the integrity of the SAJs during their fatigue life. Khashaba et al.^{16,24} found that the U_p has a linear inverse relationship with E' . The U_p values are increased with σ_{max} due to increasing the thermal and mechanical damages in the joint.

Khashaba et al.^{16,24} found that the evolution of U_p versus N/N_f of the SAJs is more pronounced compared to the E' . They have attributed this phenomenon to the lower damage rate in the SAJs during their life, which result in lower rate of stiffness reduction in comparison to the magnified area under the loading curve of the hysteresis loop (U_p). They have pointed out that the relationship of the U_p with N/N_f can be modeled better than the dynamic stiffness for predicting the life of the joint and help in preventing their catastrophic failure.

Zhang stiffness degradation model, equation (24), was modified for predicting the increase in U_p during the joint life as follows

$$\frac{U_p(N)}{U_p(0)} = \left(\frac{N \cdot k^m}{V - N} \right)^{\frac{1}{m}} \quad (26)$$

where $U_p(N)$ is the potential energy related to the N^{th} fatigue cyclic, $U_p(0)$ is the potential energy of first loading cycle, and k , m , V are parameters that determined by fitting equation (26) into the measured results.

Figure 20(a) shows the variation of the experimental and predicted normalized potential energy ($U_p(N)/U_p(0)$) as a function of normalized fatigue cycles (N/N_f) of the SiC-SAJs at different stress levels. The potential energy was normalized by its initial value $U_p(0)$. It is obvious from Figure 20(a) that the values of the normalized potential energy were increased with the increase of the stress level as

Table 6. Comparison between the researchers' finding related to the damping factor ($\tan \delta$) with current study.

Material	Test conditions	Damping factor (%)	Reference
SAJs with SiC-nanocomposite adhesive layer	10 Hz and stress ratio of 0.1	≈0.02–0.11	Current study
SAJs with Al_2O_3 -nanocomposite adhesive layer	10 Hz and stress ratio of 0.1	≈0.03–0.15	16
SAJs with neat epoxy adhesive layer	10 Hz and stress ratio of 0.1	≈0.02–0.045	21
SLJ	5 Hz and stress ratio of 0.1	≈0.02	29
SLJ	Free vibration decay method	≈0.5	53
SLJ	Free vibration decay method	≈0.01	54
SLJ	Free vibration decay method	0.1	55

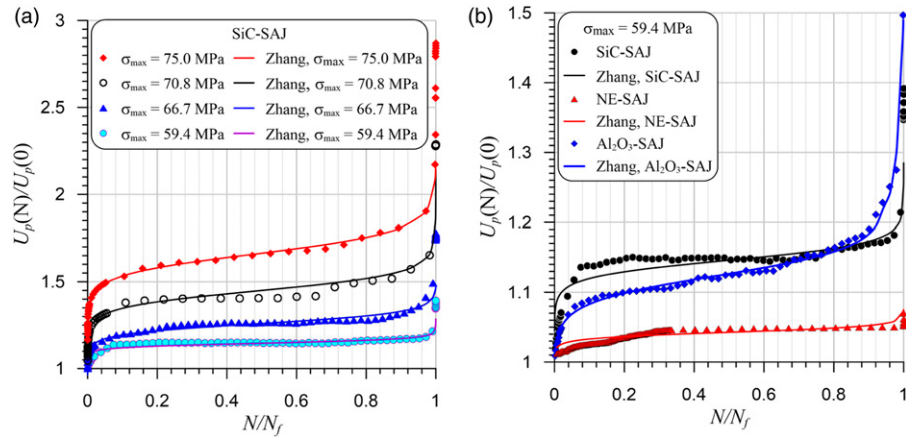


Figure 20. Experimental and predicted normalized U_p versus N/N_f : (a) SiC-SAJs at various σ_{max} , and (b) NE, SiC, and Al_2O_3 -SAJs at σ_{max} of 59.4 MPa, as representative example.

a result of decreasing the storage modulus (E'). Khashaba et al.^{16,24} found that the U_p has a linear inverse relationship with the E' . They have attributed the increase in U_p and decrease of E' with σ_{max} to the increase of thermal and mechanical interfacial damages in the SAJs. It is evident from Figure 20(a) that Zhang model predicts well the experimental measurements of the U_p , specially at higher stress levels (i.e., high damage) at which the normalized potential energy in stage II, follow a sigmoid curve with constant increasing rate during the most lifetime of the joint. Accordingly, the U_p can be considered a powerful tool for monitoring and detecting the damage in the adhesive joints in which the variation in the area enclosed by the hysteresis cycle is too small to cause a large change in the U_d , E'' and $\tan \delta$.

Figure 20(b) depicts the variation of the experimental and predicted normalized potential energy with N/N_f of NE, SiC, and Al_2O_3 -SAJs at σ_{max} of 59.4 MPa, as a representative example at lower stress level. The results in this figure indicate that Zhang model predicts well the normalized potential energy of the Al_2O_3 -SAJs compared to both NE and SiC-SAJs. Again, this result may be attributed to the lower interfacial bond strength between the Al_2O_3 -nanoparticles and the Epoxy adhesive as well as between the nanocomposite adhesive and the CFs. Therefore, the potential energy exhibited increasing rate during stage II that agrees well with Zhang sigmoid model. This behavior consistent with the lower fatigue lives (Figure 7), higher ratcheting strains (Figure 11(b)), larger enclosed area by the hysteresis loops (Figure 15(c)), and lower stiffness (Figure 17) of the Al_2O_3 -SAJs compared to the SiC-SAJs.

On the other hand, the predicted normalized potential energy of both NE and SiC-SAs show relatively less agreement with the experimental results, as shown in Figure 20(b). Again, this behavior was attributed to the

insignificant loss in the joint stiffness during stage II (main portion of joint life) that contrary to Zhang sigmoid model assumption. Hence, many efforts are required to develop analytical models that capable to monitoring and predicting the variation in the stiffness degradation as well as the increasing rate in the potential energy under low or moderate fatigue loading and thus, help in preventing the catastrophic failure of the joint without warning.

Conclusions

In this study, fatigue results of the scarf adhesive joints (SAJs) fabricated using neat epoxy (NE), and SiC and Al_2O_3 -nanocomposite adhesives were extensively analyzed regarding the effect of the adhesive materials, bond thickness (0.17 mm and 0.25 mm) on fatigue lives and dynamic behavior. The scatter in the fatigue life was investigated using the two parameter Weibull function. Safe fatigue lives of the NE, SiC, and Al_2O_3 -SAJs were estimated at different reliability levels. The following conclusions are drawn from this study.

The measured potential energy (area under loading curve) was increased with the increase of the stress level (σ_{max}) as consequence of increasing the thermal and mechanical interfacial damages in the SAJs. This result is consistent with decreasing the storage modulus (E'), which has a linear inverse relationship with Potential energy (U_p).

Potential energy (U_p) was used for the first time (except author works) for monitoring and predicting the damage in the adhesive joints in which the variation in the area enclosed by the hysteresis loop is too small to cause a large change in the factor ($\tan \delta$), loss modulus (E''), and dissipated energy (U_d).

Zhang model predicts well the experimental measurements of the potential energy and storage modulus (E') specially at higher stress levels (i.e., high damage) at which

they follow a sigmoid curve with constant increasing/decreasing rates during the most lifetime of the joint.

At lower stress level ($\sigma_{max} = 59.4$ MPa), the potential energy of the Al_2O_3 -SAJs exhibited increasing rate during stage II that agrees well with Zhang sigmoid curve compared to both NE and SiC-SAJs. This behavior consistent with the lower fatigue lives, higher ratcheting strains, larger enclosed area by the hysteresis loops, and lower stiffness of the Al_2O_3 -SAJs compared to the SiC-SAJs. Many efforts are required to develop analytical models that capable to monitoring and predicting the variation in the stiffness degradation as well as the increasing rate in the potential energy under low or moderate fatigue loading and thus, help in preventing the catastrophic failure of the joint without warning.

Reducing the adhesive layer thickness from 0.25 mm to 0.17 mm result in enhancing the tensile strength and stiffness of the SiC-SAJs by 9.6% and 4.4%, respectively, in return of 9.5% and 5.4% for the Al_2O_3 -SAJ relative to the NE-SAJs. The strength and stiffness of the SiC-SAJs with 0.17 mm bond thickness are higher than those of the Al_2O_3 -SAJ by 15.4% and 3.3%, respectively. The highest improvement of 22.0% in the fatigue strength was occurred due to incorporating SiC-nanoparticles into the bonded layer with 0.17 mm thickness in return of 4.8% for the Al_2O_3 -SAJ.

Damping factor of the NE-SAJs is marginally increased with the stress levels compared to the aggravated increase of both SiC and Al_2O_3 -SAJs. This is attributed to the more dissipated energy in developing interfacial microcrack initiation and propagation around the nanoparticles as demonstrated by the SEM images of the corrugated fractured surface.

It worth noting that the S-N curve of the SiC-SAJs at the higher reliability level (99%) is higher than that at 50% survival of the Al_2O_3 -SAJs. The estimated fatigue life of SAJs at different reliability levels are of considerable value to the designer particularly, if the structure comprises a critical component where any failure is catastrophic.

Declaration of conflicting interests

The author(s) declared no potential conflicts of interest with respect to the research, authorship, and/or publication of this article.

Funding

The author(s) disclosed receipt of the following financial support for the research, authorship, and/or publication of this article: This project was supported by the Deanship of Scientific Research (DSR) at King Abdulaziz University, Jeddah, under grant No. (G: 64-135-1443). The authors, therefore, acknowledge with thanks DSR for technical and financial support.

ORCID iD

Usama A. Khashaba  <https://orcid.org/0000-0002-7148-2807>

References

- Shiino MY, Cipó TCG, Donadon MV, et al. Waste size and lay up sequence strategy for reusing/recycling carbon fiber fabric in laminate composite: mechanical property analysis. *J Compos Mater* 2021; 55(28): 4221–4230
- Huang S, Fu Q, Yan L, et al. Characterization of interfacial properties between fibre and polymer matrix in composite materials-A critical review. *J Mater Res Technol* 2021; 13: 1441–1484.
- Selvan RT, Raja PCV, Mangal P, et al. Recycling technology of epoxy glass fiber and epoxy carbon fiber composites used in aerospace vehicles. *J Compos Mater* 2021; 55(23): 3281–3292.
- Damghani M, Bakunowicz J and Murphy A. Understanding the influence of laminate stacking sequence on strain/stress concentrations in thin laminates at repair holes with large scarf angles. *J Compos Mater* 2019; 53(28–30): 4273–4284.
- Javaid U, Ling C and Cardiff P. Mechanical performance of carbon-glass hybrid composite joints in quasi-static tension and tension-tension fatigue. *Eng Fail Anal* 2020; 116: 104730.
- Bonhin EP, David-Müzel S, Alves MC, et al. A review of mechanical drilling on fiber metal laminates. *J Compos Mater* 2021; 55(6): 843–869.
- Khashaba UA. A novel approach for characterization of delamination and burr areas in drilling FRP composites. *J. composite structures* 2022; 290: 115534. In press
- Wu F and Yao W. A fatigue damage model of composite materials. *Int J Fatigue* 2010; 32: 134–138
- Moreira RDF, de Moura MFSC, Silva FGA, et al. High-cycle fatigue analysis of adhesively bonded composite scarf repairs. *Composites Part B Eng* 2020; 190: 107900
- Shenoy V, Ashcroft IA, Critchlow GW, et al. An investigation into the crack initiation and propagation behaviour of bonded single-lap joints using backface strain. *Int J Adhes Adhes* 2009; 29(4): 361–371
- Paygozar B and Sadigh MAS. Adhesively bonded aluminum double-strap joints improved by nano-silica. *Trans Indian Inst Met* 2020; 73: 1401–1406
- Maravina L and Linul E. Fracture toughness of rigid polymeric foams: a review. *Fatigue Fract Engng Mater Struct* 2020; 43(11): 2483–2514
- Zamani P, Jaamiahmadi A and da Silva LFM. The influence of GNP and nano-silica additives on fatigue life and crack initiation phase of Al-GFRP bonded lap joints subjected to four-point bending. *Compos Part B Eng* 2021; 207: 108589
- Chavoshian M, Kamali R, Tutunchi A, et al. Effect of silicon carbide nanoparticles on the adhesion strength of steel–epoxy composite joints bonded with acrylic adhesives. *J Adhes Sci Technol* 2017; 31: 345–357
- Khashaba UA, Aljinaidi AA and Hamed MA. Nanofillers modification of epocast 50–A1/946 epoxy for bonded joints. *Chin J Aeronaut* 2014; 27: 1288–1300

16. Khashaba UA. Dynamic analysis of scarf adhesive joints in CFRP composites modified with Al₂O₃-nanoparticles under fatigue loading at different temperatures. *Compos Part A-Appl S* 2021; 143: 106277
17. Shahani AR and Pourhosseini SM. The effect of adherent thickness on fatigue life of adhesively bonded joints. *Fatigue Fract Eng. Mater Struct* 2019; 42(2), 561–571
18. Liao L, Huang C and Sawa T. Effect of adhesive thickness, adhesive type and scarf angle on the mechanical properties of scarf adhesive joints. *Int J Sol Struct* 2013; 50: 4333–4340
19. Rafiee R and Hashemi-Taheri MR. Failure analysis of a composite wind turbine blade at the adhesive joint of the trailing edge. *Eng Fail Anal* 2021; 121: 105148
20. Khashaba UA, Aljinaiidi AA and Hamed MA. Fatigue and reliability analysis of nano-modified scarf adhesive joints in carbon fiber composites. *Compos Part B Eng* 2017; 120: 103–117
21. Khashaba UA. Dynamic analysis of scarf adhesive joints in carbon-fiber composites at different temperatures. *AIAA J AIAA J* 2020; 58: 4142–4157
22. Khashaba UA, Aljinaiidi AA and Hamed MA. Analysis of adhesively bonded CFRE composite scarf joints modified with MWCNTs. *Compos Part A-Appl S* 2015; 71: 59–71
23. Khashaba UA. Static and fatigue analysis of bolted/bonded joints modified with CNTs in CFRP composites under hot, cold and room temperatures. *Compos Struct* 2018; 194: 279–291
24. Khashaba UA, Najjar IMR and Almitani KH. Failure analysis of scarf adhesive joints modified with SiC-nanoparticles under fatigue loading. *Compos Sci Technol* 2022; 221: 109301
25. Beber VC, Baumert M, Klapp O, et al.. Fatigue failure criteria for structural film adhesive bonded joints with considerations of multiaxiality, mean stress and temperature. *Fatigue Fract Engng Mater Struct* 2021; 44(3): 636–650
26. Olajide SO and Arhatari BD. Progress on interacting fatigue, creep & hysteretic heating in polymer adhesively bonded composite joints. *Int J Fatigue* 2017; 98: 68–80
27. Ameur MB, El Mahi A, Rebire J-L, et al. Experimental fatigue behavior of carbon/flax hybrid composites under tensile loading. *J Compos Mater* 2021; 55(5): 581–596
28. Ahmadzadeh GR and Varvani-Farahani A. Ratcheting prediction of Al 6061/SiCP composite samples under asymmetric stress cycles by means of the Ahmadzadeh-Varvani hardening rule. *J Compos Mater* 2016; 50(17): 2389–2397
29. Bourchak M, Algarni A, Khan A, et al. Effect of SWCNTs and Graphene on the fatigue behavior of antisymmetric GFRP laminate. *Compos Sci Technol* 2018; 167: 164–173.
30. Malloum A, El Mahi A and Idriss M. The effects of water ageing on the tensile static and fatigue behaviors of greenepoxy-flax fiber composites. *J Compos Mater* 2019; 53: 2927–2939
31. Idriss M and El Mahi A. Effects of debonding length on the fatigue and vibration behaviour of sandwich composite. *J Compos Mater* 2017; 51(13): 1839–1847
32. Mactabi R, Rosca ID and Hoa SV. Monitoring the integrity of adhesive joints during fatigue loading using carbon nanotubes. *Compos Sci Technol* 2013; 78: 1–9
33. Afendi M, Teramoto T and Bakri HB. Strength prediction of epoxy adhesively bonded scarf joints of dissimilar adherends. *Int J Adhes Adhes* 2011; 31(6): 402–411
34. Davies P, Sohier L, Cognard J-Y, et al. Influence of adhesive bond line thickness on joint strength. *Int J Adhes Adhes* 2009; 29: 724–736
35. Adin H. The effect of angle on the strain of scarf lap joints subjected to tensile loads. *Appl Math Model* 2012; 36: 2858–2867
36. Nakano H, Omiya Y, Sekiguchi Y, et al. Three-dimensional FEM stress analysis and strength prediction of scarf adhesive joints with similar adherends subjected to static tensile loadings. *Int J Adhes Adhes* 2014; 54: 40–50
37. Kwon B, Choe H, Jeong J, et al. Static and fatigue behavior of induction-welded single lap carbon fiber reinforced polyetherketoneketone thermoplastic composite joints. *J Compos Mater* 2021; 55(28): 4183–4193
38. Khashaba UA. Fatigue and reliability analysis of unidirectional GFRP composites under rotating bending loads. *J Compos Mater* 2003; 37: 317–331
39. Tanimoto T., Amijima S. and Ishikawa H.. *A Reliability Analysis Approach to Fatigue Life Dispersion of Laminated Glass Fiber Composite Materials*, 33. Cambridge, England: ICM, 1979, pp. 207–216
40. Adamczyk WP, Pawlak S and Ostrowski Z. Determination of thermal conductivity of CFRP composite materials using unconventional laser flash technique. *Measurement* 2018; 124: 147–155
41. Goel A, Chawla K K, Vaidya U K, et al. Characterization of fatigue behavior of long fiber reinforced thermoplastic (LFT) composites. *Mater Charact* 2009; 60: 537–544
42. Olajide SO and Arhatari BD. Recent progress on damage mechanisms in polymeric adhesively bonded high-performance composite joints under fatigue. *Int J Fatigue* 2017; 95: 45–63
43. Prasad EV, Sivateja C and Sahu SK. Effect of nanoalumina on fatigue characteristics of fiber metal laminates. *Polym Test* 2020; 85: 106441
44. Jiang Z, Wan S, Fang Z, et al. Experimental investigation of fatigue behavior for adhesively-bonded GFRP/steel joints. *Eng Struct* 2020; 213: 110580
45. Zhang Y, Vassilopoulos AP and Keller T. Stiffness degradation and fatigue life prediction of adhesively-bonded joints for fiber-reinforced polymer composites. *Int J Fatigue* 2008; 30: 1813–1820
46. Shanmugam V, Das O, Babu K, et al. Fatigue behaviour of FDM-3D printed polymers, polymeric composites and architected cellular materials. *Int J Fatigue* 2021; 143: 106007

47. Ding J and Cheng L. Ultra-high three-point bending fatigue performance of nano-silica-reinforced CFRP. *Int J Fatigue* 2021; 145: 106085
48. Tareq MS, Jony B, Zainuddin S, et al. Fatigue analysis and fracture toughness of graphene reinforced carbon fibre polymer composites. *Fatigue Fract Engng Mater Struct* 2021; 44(2): 461–474
49. Barron V, Buggy M and Mckenna NH. Frequency effects on the fatigue behavior on carbon fibre reinforced polymer laminates. *J Mater Sci* 2001; 36: 1755–1761
50. Li LB, Reynaud P and Fantozzi G. Tension-tension fatigue behavior of unidirectional SiC/Si3N4 composite with strong and weak interface bonding at room temperature. *Ceramics Int* 2017; 43: 8769–8777
51. Alva A and Raja S. Dynamic characteristics of epoxy hybrid nanocomposites. *J Reinf Plast Comp* 2011; 30: 1857–1867
52. Khashaba UA and Najjar IMR. *A New Approach for Fatigue Damage Detection in Adhesive Joints Modified with Nanoparticles in CFRP Composites under Different Temperatures*. Fatigue Fract Eng Mater Struct, 2022. <https://doi.org/10.1111/ffe.13698>
53. Gunawan S and Gibson RF. Analytical and experimental characterization of extensional damping in single lap visco-elastic adhesive joints. 28th Structures, Structural Dynamics and Materials Conference, Paper No. AIAA-87-0886-CP, Monterey, CA, April 6–8, 1987.
54. Adams RD, Cooper DGA and Pearson S. Vibration damping of adhesively bonded joints. In: da Silva L., Öchsner A. and Adams RD., Hrsg: (eds). *Handbook of Adhesion Technology*. Springer-Verlag Berlin Heidelberg; 2011.
55. Araújo HAM, Machado JJM, Marques EAS and Da Silva LFM. Dynamic behaviour of composite adhesive joints for the automotive industry. *Compos Struct* 2017; 171: 549–561

Appendix

Notation

N_f	fatigue life
N	cycle number
E''	loss modulus
E'	storage modulus
U_d	dissipated energy
U_p	potential energy
η	$\tan \delta$ (loss factor)
ζ	damping ratio
RS	ratcheting strain
ε_{max} , ε_{min} and ε_a	maximum, minimum, and amplitude of the hysteresis strains cycle
σ_{max} , σ_{min} and σ_a	maximum, minimum, and amplitude of the hysteresis stress cycle
E_{Dyn}	dynamic modulus
t_a	bondline thickness
$D(N)$	fatigue damage index
k , m , V	model parameters
k , a and b	coefficients
θ	cycle angle (0 to 2π)

h	horizontal shift angle.
δ	phase shift angle
$f(N_f)$	Weibull probability density function
$P(N_f)$	probabilities of failure
$P_s(N_f)$	probabilities of survival
i	failure order
α	shape parameter of Weibull function
β	Scale parameter of Weibull function
CV	coefficient of variation
n	total number of samples for each fatigue test
Γ	gamma function
N_f	fatigue life
N_{fp}	predicted fatigue lives
N_m	mean life
N_R	safe design fatigue life
\tilde{N}	characteristic life
N_y	lower bound life
S_M , S_N , and S_R	sample size, fleet size and reliability scatter factors.
X^2_γ ($2m$)	chi-square distribution with $2m$ degree of freedom.